Dawn-dusk asymmetries in the auroral particle precipitation and their modulations by substorms

Simon Wing[1], Jay R. Johnson[2], and Enrico Camporeale[3]

[1]Applied Physics Laboratory, The Johns Hopkins University, Laurel, Maryland, USA

[2]Princeton Plasma Physics Laboratory, Princeton University, Princeton, New Jersey, USA

[3]Center for Mathematics and Computer Science (CWI), Amsterdam, The Netherlands

Abstract. Auroral particle precipitation exhibits dawn-dusk asymmetries that reflect the asymmetries in the particle populations, waves, and processes in the magnetosphere. The diffuse auroral electrons can be observed mainly in 22:00 – 09:00 MLT, which coincides much with the spatial distribution of the whistler-mode chorus waves that have been shown to be the predominant mechanism for pitch-angle scatterring magnetospheric electrons into the loss cone. On the other hand, the monoenergetic auroral electrons can be observed at dusk-midnight sector. The monoenergetic electrons are magnetospheric electrons that have gone through a quasi-static parallel electric field in the upward field-aligned current regions. The broadband auroral electrons can be found mostly at 22:00 – 02:00 MLT where a peak in the Poynting flux of Alfvén waves is observed. Alfvén waves are known to cause broadband acceleration of electrons. There may be a connection between monoenergetic and broadband electrons in that the low frequency Alfvén wave–electron interaction can result in monoenergetic electron signature. Substorms increase the power of the diffuse, monoenergetic, and broadband electron aurora by 310%, 71%, and 170%, respectively. The duration of the substorm cycle for monenergetic and broadband auroral is ~5 hr, but it is larger than 5 hr for diffuse auroral electrons.

Keywords: particle precipitation, diffuse aurora, broadband aurora, monoenergetic aurora, ion aurora, substorm cycle.

Index terms: 2704, 2790, 2407, 2455, 2483

Key points: (1) Broadband aurora increases at substorm onset, but it decreases rapidly 15 min after onset. (2) Monoenergetic aurora start increasing approximately 75 min before the substorm onset. (3) Monoenergetic and broadband electron aurorae complete the substorm cycle within 5 hr. (4) Diffuse electron aurora peak at 1 hr after the substorm onset.

1. Introduction

The Earth's magnetic field lines converge in the northern and southern polar regions. Ions and electrons in the magnetosphere follow the magnetic field. Downgoing particles, that are closely field-aligned, precipitate into the high latitude ionosphere. As a result, the particle precipitation detected within the auroral oval can serve as a window to the magnetosphere.

In the magnetosphere, the magnetic field strength, and the ion and electron temperatures increase with decreasing distance from Earth. Where the magnetic field is sufficiently strong or the particle (ion and electron) temperatures are sufficiently high, typically at distance $r < 10 – 12$ Re, the curvature and gradient drifts, which are temperature dependent, can play a significant role in the transport of ions and electrons [e.g., *Wang et al*., 2004]. The curvature and gradient drifts move hotter ions westward and hotter electrons eastward, leading to dawn-dusk asymmetries in the near-Earth plasma sheet and the inner magnetosphere. The ion temperatures are higher at dusk-midnight sector than at midnight-dawn sector during the quiet time and substorm growth phase [e.g., *Spence and Kivelson*, 1993; *Wing and Newell*, 2002; *Wing et al*., 2005; *Johnson and Wing*, 2009; *Wang et al*., 2001; 2006; 2011]. The electron temperatures exhibit the opposite asymmetries with the temperature being higher at the midnight-dawn sector than at the dusk-midnight sector. These dawn-dusk asymmetries can also manifest in the auroral ion and electron precipitation in the ionosphere [e.g., *Newell et al*., 2010; *Wing et al*., 2013].

The dawn-dusk asymmetries of the auroral particle precipitation can also be modulated by substorms, which inject into and energize particles at the inner magnetosphere. There are generally three phases of a substorm: growth, expansion, and recovery [e.g., *Tanskanen et al*., 2002; *Lui*, 1991]. The growth phase typically begins in the quiescent period at the time of the southward turning of the interplanetary magnetic field (IMF) and ends at the onset of the expansion phase (commonly referred to as the substorm onset), which is an interesting topic in its own right (e.g., *Lyons et al.*, [1997], *Birn and Hones* [1981], *McPherron* [1991], *Hsu and McPherron* [2004], *Meng and Liou* [2004], *Rostoker* [2002], *Lui* [2004], *Angelopoulos et al.* [2008], *Haerendel* [2010], *Sergeev et al.* [2012], *Johnson and Wing* [2014]). During the growth phase, the auroral oval expands equatorward, the aurora and the electrojet gradually intensify, the plasma sheet thins, and the magnetospheric magnetic field lines stretch (become tail-like), as the solar wind energy is stored in the magnetotail. During the expansion phase the auroral oval brightens and expands poleward, eastward, and westward, the westward electrojet significantly increases, and the magnetic field configuration in the inner plasma sheet changes rapidly from the stretched tail-like configuration to a more dipolar configuration. The expansion phase is followed by the recovery phase, during which the magnetosphere returns back to its original undisturbed state. The start of the recovery phase is usually signaled by the waning of the substorm aurora and weakening of the westward electrojet. The recovery phase ends when the magnetosphere reaches its normal undisturbed state.

In the present paper, the dawn-dusk asymmetries in the auroral ion and electron precipitation and how these asymmetries change throughout the substorm phases are presented. The time scales for the substorm cycle and each substorm phase are examined. We categorize the electron precipitation into three categories based on their spectra: diffuse, monoenergetic, and broadband auroral electrons [e.g., *Newell et al.*, 2009; 2010; *Wing et al.*, 2013]. These are described in Sections 2 – 4. The diffuse auroral electrons are most likely downgoing field-aligned plasma sheet electrons that precipitate in the ionosphere. The electrons in the loss cone (the field-aligned electrons) are replenished by the pitch angle scattering resulting primarily from electron interactions with the very low frequency (VLF) whistler-mode chorus waves [e.g., *Thorne*, 2010; *Reeves et al.*, 2009; *Summers et al.*, 1998; *Ni et al.*, 2011]. When precipitating electrons exhibit an intense and broad energy spectrum, they are classified as broadband. This electron population is believed to primarily result from acceleration by Alfvén waves [*Chaston et al.*, 2002; 2003; 2008], which are often observed around the time of substorm dipolarization [*Lessard et al.*, 2006]. Monoenergetic electron spectra, on the other hand, likely indicate the presence of a parallel electric field that accelerates the electrons downward and are usually related to the global upward currents. The monoenergetic electrons may also result from the electron interaction with low frequency Alfvén waves/ballooning modes that accelerate electrons [e.g., *Pritchett and Coroniti*, 2010; *Damiano and Johnson*, 2012]. Precipitating ions are magnetospheric ions that have been pitch angle scattered into the loss cone by current sheet scattering [e.g., *Speiser*, 1965; *Lyons and Speiser*,1982; *Sergeev et al.*, 1983; 1993] and/or interaction with electromagnetic ion cyclotron (EMIC) waves [e.g., *Jordanova et al.*, 2001; *Sergeev et al.*, 2015]. Thus, these ions and the three types of electron spectra can provide information about the particle populations, waves, and processes in the magnetosphere.

2. Diffuse electron aurora

Figure 1 presents energy flux maps from diffuse auroral electrons obtained from the SSJ4/5 particle detector on board of DMSP F12 – F16 satellites in the interval 1996 – 2007. The SSJ4/5 can detect ions and electrons with energy range of 30 eV – 30 keV. The DMSP satellites are in sun-synchronous, nearly circular polar orbits at approximately 845 km altitude. The SSJ4/5 detector apertures always point toward local zenith, which means that at high latitudes, only highly field-aligned precipitating particles well within the atmospheric loss cone are observed. The substorm onset times are taken from two substorm databases: (1) the Polar UVI substorm database [*Liou et al*., 1997; 2001] and (2) the IMAGE substorm database [*Frey et al*., 2004]. Only isolated substorms that are separated by at least 5 hr from other substorms are used to construct the figure. Out of 4861 substorm events in the original combined dataset, 1677 events, or about 34%, fall into this isolated substorm category. The diffuse electrons typically have a Kappa distribution in the magnetotail [*Christon et al*., 1991; *Kletzing et al*., 2003]. However, in order not to leave out any electrons, the electrons that are not classified as either monoenergetic or broadband (see Sections 3 and 4) are also classified as diffuse.

Figure 1 shows that the diffuse auroral electron energy flux increases around substorm onset, consistent with the finding in *Newell et al*. [2010]. However, Figure 1 also shows that after onset, the energy flux continues to increase and remains at an elevated level for at least 2 hr after onset, reaching a maximum at about 1 hr after onset (this can be seen more easily in Figure 7, which is discussed in Section 6). Moreover, it appears that at and after onset, the increase of the diffuse electron energy flux is confined approximately in the sector spanning 22:00–09:00 MLT. This dawn-dusk asymmetry is discussed further in Section 8.

The diffuse electrons are the magnetospheric electrons that precipitate into the loss cone in the ionosphere. As the plasma sheet electrons **E** × **B** convect earthward, they also curvature and gradient drift eastward toward dawn. The field-aligned component of these electrons are quickly lost through the lost cone, but they are replenished by pitch-angle scattering. A leading mechanism for pitch-angle scattering is VLF whistler-mode chorus wave–electron interactions [e.g., *Thorne*, 2010; *Reeves et al*., 2009; *Summers et al*., 1998; *Camporeale,* 2015*; Camporeale et al.,* 2015]. Upper band chorus waves provide the dominant scattering process for electrons 100 eV – 2 keV, while lower band chorus waves are most effective for scattering electrons > ~2keV [*Ni et al.*, 2011]. Electrostatic electron cyclotron harmonic (ECH) waves can also pitch angle scatter electrons, but *Ni et al*. [2011] found that ECH wave scattering rates are at least one order of magnitude smaller than those by whistler-mode chorus waves. Studies have shown that whistler-mode chorus waves are excited in the region spanning premidnight to noon, which includes the region where the diffuse electrons are observed, at 22:00–09:00 MLT. This can be seen in Figure 2, which shows the whistler-mode chorus wave and diffuse electron spatial distributions. Around 09:00 MLT, the diffuse electron flux decreases, which may suggest that the whistler-mode chorus waves start weakening. In the magnetosphere, the electrons continue to drift eastward, circling the earth, but they are only observed in the ionosphere as diffuse electrons when and where there are whistler-mode chorus waves to pitch-angle scatter them. Because the bounce motion is generally faster than the drift motion, the signatures of the waves in the ionosphere can be mapped to the magnetosphere at the same MLT. Whistler mode chorus waves are important for the study of radiation belts because they have been found to contribute to both energy and pitch angle diffusion [*Li et al*., 2007; *Horne and Thorne*, 2003].

3. Broadband electron aurora

The precipitating electrons are classified as broadband electrons if three or more energy channels have differential energy flux (dJ_E/dE) > 2.0×10^8 (eV cm^{-2} s^{-1} sr^{-1} eV^{-1}). There are some caveats, which are listed in *Newell et al.* [2010] and are not repeated here. Figure 3 displays the broadband electron energy flux maps for 1 hr before onset through 1 h and 45 min after onset in the same format as in Figure 1. The database and methodology used to construct Figure 3 are also similar as those used to construct Figure 1 and are briefly discussed in Section 2. The broadband aurora rises after onset in the 21:00–02:00 MLT interval and appears to wane or to start waning approximately 15 min after onset.

Broadband aurora is characterized by precipitating electrons having a broad energy spectrum. Such precipitation is thought to result from electron interaction with dispersive Alfvén waves when their frequency is comparable to the electron transit time [*Chaston et al*., 2002, 2003, 2007; 2008; *Damiano et al*., 2015]. Typical Poynting fluxes in Alfvén waves at high latitude have been shown sufficient to account for 30-35% of auroral luminosity [*Wygant et al.*, 2002; *Keiling et al.*, 2002; 2003]. Figure 4 shows that the statistical local time distribution of Alfvén waves is similar to that of the broadband electrons.

The association of Alfvén waves, substorm, and broadband electrons has been made by *Lessard et al*. [2006]. The paper notes a connection between dipolarization events observed in the magnetotail and dispersive Alfvén waves observed above the ionosphere, which are associated with the broadband electron precipitation. Observations of Pi1B (irregular bursty pulsations with periods from 1 to 40 sec) were detected by GOES 9, FAST, and at the ground in conjunction with a substorm. While GOES detected compressional magnetic field fluctuations along with dipolarization at geosynchronous orbit, FAST (which was conjugate to GOES) detected shear Alfvén waves as a broad band ELF wave spectrum. The ratio of $\delta E/\delta B$ for the waves was consistent with Doppler-shifted dispersive Alfvén waves that have been reported [*Stasiewicz et al.*, 2000; *Chaston et al.*, 2008], suggesting that compressional waves mode convert to dispersive shear Alfvén waves in this region. These same waves were also observed by ground-based magnetometers on conjugate field lines.

Because transfer of energy by Alfvén waves is most efficient when the perpendicular wavelength is small [*Hasegawa*, 1976; *Lysak and Song*, 2003; *Damiano et al*., 2007], it is additionally necessary that there be cascade of energy from large scales to small scales [*Chaston et al*., 2008]. Cross-scale coupling may result from linear phase mixing in inhomogeneity

[Lysak and Song, 2011; *Camporeale et al*., 2012], nonlinear wave-wave cascade [*Vasconez et al*., 2014; *Schekochihin et al*., 2009 and references therein] or by nonlinear wave-particle interactions [*Damiano and Johnson*, 2012].

Electrons with broadband energy distribution are consistent with acceleration in a time-varying parallel electric field [*Chaston et al*., 2002] that is associated with small-scale dispersive Alfvén waves. Electrons can be resonantly trapped in the wave potential of an Alfvén wave pulse [*Kletzing*, 1994] typically leading to the development of a velocity-dispersed beam in front of the pulse [*Watt et al*., 2005]. At lower altitude, the electrons escape the potential well and precipitate into the ionosphere as an energy-dispersed population [*Watt and Rankin*, 2009].

In the transient response models [e.g., *Nishida*, 1979; *Kan et al*., 1982; *Hull et al*., 2010], the magnetospheric reconfiguration and diversion of the cross-tail currents by the current wedge are communicated to the ionosphere by Alfvén waves. The broadband aurora that results from the initial substorm pulse may be expected to last a few Alfvén bounce periods because Alfvén waves damp kinetically on electrons absorbing most of the wave energy after a few reflections via wave-particle interactions [*Lysak and Song*, 2003; *Damiano and Johnson*, 2012] and/or Joule dissipation in the ionopshere [*Hull et al*., 2010].

As shown in Figure 3, broadband auroral power peaks following onset and remains elevated for about 15 minutes, consistent with the decay time of Alfvén waves. As shown later in Sections 6 and 7, the broadband auroral power reaches its half maximum value in ~40 min from the time it reaches its maximum value (the end of the expansion phase), which gives a measure of how fast the auroral power and Alfvén waves decay. After the rapid decay of the main Alfvén waves in the interval 15–45 min after onset, there seems to be residual Alfvén waves that slowly decay starting at approximately 45 min after onset (as can be seen later in

Figure 7b).

4. Monoenergetic electron aurora

The algorithm for classifying monoenergetic electrons is as follows. (1) Identify the differential energy flux peak, and subsequently look at the drops one and two energy channels above and below the peak. If the differential energy flux drops to 30% or less of the peak within these two steps (at energies above and below the peak), then the event is considered monoenergetic. (2) The differential energy flux must be above 1.0×10^8 (eV cm^{-2} s^{-1} sr^{-1} eV^{-1}) at the peak channel. (3) If either the average energy is below 80 eV or the differential energy flux peak is below 100 eV, the spectrum is not considered "accelerated." Such events may result from spacecraft charging (low acceleration potentials are excluded by this rule).

The monoenergetic auroral electron energy flux map can be constructed using the same dataset and methodology described in Section 2. Figure 5 shows the monoenergetic auroral electron energy flux in the same format as in Figures 1 and 3. Many of its features are quite different from those in the diffuse and broadband aurorae. The monoenergetic aurora is concentrated mainly in the dusk-midnight sector. The monoenergetic auroral electron energy flux starts increasing approximately 1 hr and 15 min before onset and increases more significantly at substorm onset, reaching a maximum at 15 min after onset. This can be more clearly seen in Figure 7c and discussed in Section 6.

The monoenergetic electron energy flux reaches a minimum 1 hr and 15 min before onset (as can be seen later in Figure 7c) and increases thereafter, suggestive of a correlation between monoenergetic electron precipitation and the growth phase magnetic field configuration. As the tail stretches during the growth phase, field-aligned currents intensify [*McPherron*, 1972;

Watanabe and Iijima, 1993; *Wing and Sibeck*, 1997; *Tsyganenko and Sibeck*, 1994; *Tsyganenko et al.*, 1993; *Zanetti and Potemra*, 1986]. In the upward field-aligned current regions, the current-voltage relationship implies that the parallel potential drop would increase in order to maintain higher currents by drawing more electrons downward [*Knight*, 1973]. Hence, an increase in the monoenergetic electron aurora may simply be an indicator of elongation of the tail that occurs during the growth phase. Figure 5 shows that the monoenergetic electrons can be observed mainly in the dusk-midnight sector. This would be consistent with the increase in the upward region-1 field-aligned current (R1) in the dusk-midnight sector during the growth phase. In the midnight-dawn sector, R1 may also increase, but here R1 is downward and so fewer monoenergetic electrons would be expected. Region-2 field-aligned current (R2) at the midnight-dawn sector flows upward, but few monoenergetic electrons are observed at this location. This may result from the higher electron density on the dawnside than on the duskside magnetosphere due to the eastward curvature and gradient drifts of the electrons.

Another possibility for the increase in monoenergetic precipitation around substorm onset is the development of low-frequency waves that accelerate electrons, but do not lead to global instability. One such possibility is the kinetic-ballooning/interchange mode discussed by *Pritchett and Coroniti* [2010], which operates in a stretched-tail configuration with a minimum in Bz. These modes are thought to be associated with interchange heads, which generate auroral streamers and contribute to the monogenergetic electron precipitation. Many studies have shown that an auroral streamer is a fast flow signature in the ionosphere [e.g., *Nakamura et al.*, 2001; *Sergeev et al.*, 2004]. Fast flows have been attributed to reconnection leading to flux tubes having depleted total entropy (S), which initiate unstable growth of ballooning and interchange instabilities resulting in earthward propagation of flux tubes [e.g., *Birn et al.*, 2009; 2011;

McPherron et al., 2011; *Wing and Johnson*, 2009; 2010; *Wolf et al.*, 2009]. Fast flows have also been attributed to current disruption leading to field-line collapse [*Lui*, 1994; *Wolf et al.*, 2009].

Fast flows are also observed following substorm onset, in the expansion and even recovery phases. For example, *Baumjohann et al.*, [1999] shows that the earthward fast flow occurrence rate peaks between 0 and 60 min after onset depending on the GSM X location of the fast flow. The superposition of these peaks may give the broad peak in the monoenergetic auroral power seen in the interval 15–60 min after onset in Figure 7c. These fast flows can launch low frequency global Alfvén waves that are associated with monoenergetic precipitation [*Damiano and Johnson*, 2012] (the low frequency Alfvén wave connection to monoenergetic electrons is further explored in Section 9). Regardless of how they are formed, fast flows have been observed more frequently in the dusk-midnight than the midnight-dawn sector in the tail [e.g., *McPherron et al.*, 2011]. This dawn-dusk asymmetry has also been seen in RCM-Equilibrium (RCM-E) simulation and has been attributed to the ion westward curvature and gradient drifts [e.g., *Zhang et al.*, 2008]. The dawn-dusk asymmetry is discussed further in Section 8.

5. Ion Aurora

Precipitating ions are magnetospheric ions that have been pitch angle scattered into the loss cone by current sheet scattering [e.g., *Speiser*, 1965; *Lyons and Speiser*,1982; *Sergeev et al.*, 1983; 1993; *Wing et al.*, 2005] and/or interaction with electromagnetic ion cyclotron (EMIC) waves [e.g., *Jordanova et al.*, 2001; *Sergeev et al.*, 2015]. Figure 6 shows aurora ion energy flux in the same format as Figures 1, 3, and 5. Apparently, ion aurora too is enhanced after onset, but in comparison with electron aurorae of any type, the enhancement is smaller (note the different color scale with respect to the previous figures). The enhancement appears to continue for at least 1 hr and 45 min after onset as shown in Figure 6. Near the end of the growth phase, i.e., Δt = –30 to 0 min, the ion energy flux peaks at 18:00–21:00 MLT sector, which can be attributed to the ion curvature and gradient westward drifts toward dusk [e.g., *Spence and Kivelson*, 1993; *Wing and Newell*, 2002; *Wing et al*., 2005; *Johnson and Wing*, 2009; *Wang et al*., 2001; 2006; 2011].

There is also a second peak at 02:00–05:00 MLT that can be seen throughout the substorm cycle (sometimes the two peaks are close together that they can't be easily distinguished). Wing et al. [2013] shows that the ion pressure exhibits a second peak at the same location. These ion pressure and energy flux maxima can be attributed to a peak in the ion number flux (not shown). The pressure peak around 02:00–05:00 MLT in the plasma sheet has been previously observed and attributed to a density peak during active times [e.g, *Korth et al*., 1999; *Wing and Newell*, 1998] and during growth phase [*Wing et al*., 2007; *Wing and Johnson*, 2009]. The dawn density enhancement during high magnetic activity may result from the cold solar wind ion entry on the dawn flank and flow stagnation when enhanced **E** × **B** and corotation are nearly cancelled by the curvature and gradient drifts [e.g., *Friedel et al.*, 2001]. Another possible mechanism also presumes solar wind ion entry along the dawn flank, but additionally, an enhanced **E** × **B** pushing the solar wind origin ions closer to Earth where the flux tube volume is smaller and hence ions have higher density [*Wang et al.*, 2003]. Figure 6 shows that the dawn peak persists after onset. This may be associated with substorm injection and flow stagnation.

6. Quantifying the nightside electron auroral power increase by substorms

We examine the evolution of the nightside particle precipitation power quantitatively from 2 hr before onset to 3 hr after. The solid line in Figure 7a shows the diffuse electron auroral power for the entire nightside, 18:00-06:00 MLT (nightside hemispheric power), whereas the dashed line is for the midnight-dawn sector, 00:00-06:00 MLT. The procedure used to calculate these quantities is similar the one used in *Newell et al*. [2010]. The nightside diffuse auroral power increases at onset and continues to increase after onset, reaching a maximum at 1 hr after onset. The nightside diffuse auroral power spans a huge range during the substorm cycle, from approximately 1.2 GW at 15 min before onset to 4.9 GW at about 1 hr after onset. Therefore, substorm-led magnetospheric reconfiguration typically increases the diffuse auroral electron power by 310%. The nightside diffuse electron auroral power is dominated by the power in the midnight-dawn sector. As can be seen from Figure 7a, the diffuse auroral power for midnight-dawn sector (dashed line) constitutes approximately 70–80% of the power for the entire nightside (solid line). The green asterisk marks the position of half maximum power, which is based on the maximum power taken at the end of the expansion phase and the baseline power taken at 15 min before onset.

In Figure 7b, the solid line plots the broadband auroral power integrated for the entire nightside, 18:00–06:00 MLT, whereas the dashed line plots the power integrated from 21:00 to 02:00 MLT. Comparing the two curves, we can see that the power at 21:00–02:00 MLT constitutes approximately 50–75% of the total nightside power. Substorms increase the integrated power from 0.56 GW at 15 min before onset to 1.5 GW at 15 min after onset, which represents a 170% increase. The broadband aurora peaks at 15 min after onset.

In Figure 7c, the solid line plots the evolution of the nightside electron monoenergetic auroral power obtained by integrating from 18:00 to 06:00 MLT. The monoenergetic auroral power reaches a minimum at 1 hr and 15 min before onset. The monoenergetic power increases drastically at onset. After onset, the power continues to increase, but only for a short time, reaching the maximum at 15 min after onset. The nightside monoenergetic auroral power is dominated by the power in the dusk-midnight sector, 18:00–24:00 MLT, which is plotted as the dashed line in Figure 7c. From the comparison of the solid and dashed lines, it can be seen that approximately 60–75% of the monoenergetic nightside auroral power come from the dusk-midnight sector. The substorm increases the monoenergetic auroral electron power by 71% from 1.05 GW at 15 min before onset to 1.8 GW at 15 min after onset.

7. The durations of substorm cycle and phases from electron precipitation perspective

Previous studies have reported greatly varying durations for the substorm cycle and phases [e.g., *Huang et al.*, 2003; *Tanskanen et al.*, 2002; *Bargatze et al.*, 1999; *Baker et al.*, 1994; *McPherron et al.*, 1986; *Baker et al.*, 1981; *Pulkkinen et al.*, 194]. Some of these differences may be attributed, at least partly, to the differences in the instrumentations used to make observations and the locations where the observation are made. These rich and diverse observations help advance our understanding of the substorm processes. Here, we attempt to estimate timescales of the substorm phases for the three different types of electrons using the substorm events obtained from satellite UV images [*Liou et al.*, 1997; 2001; *Frey et al.*, 2004]. We define the minimum auroral power before onset as the start of the growth phase and the maximum auroral power after onset as the end of the expansion phase/start of the recovery phase.

The monoenergetic and broadband electron auroral powers complete the entire substorm cycle approximately within 5-hr. That is, 3 hr after onset, these auroral powers finally reach roughly the values to those at 2 hr before onset. On the other hand, the diffuse electron auroral power appears to require more than 5 hr to complete the cycle.

The duration of the substorm cycle has been reported to be approximately 2–3 hr [e.g., *Huang et al*., 2003] or 4 hr [e.g., *Tanskanen et al*., 2002] based on substorm onsets determined by the ground magnetic field observations or indices derived from these observations such as AE, AL or IL. So, the durations of the substorm cycle for all electron aurorae appear larger than or at the upper end of the range of the values obtained from ground magnetic field observations. For the remainder of this section, we examine the duration of each substorm phase for the three types of electrons.

The monoenergetic and broadband electron aurora growth phases start at approximately 1 hr and 15 min before onset, when the power reaches the minimum. The growth phase signature for the diffuse electron aurora is not so clear. The minimum at 15 min before onset in the diffuse auroral power in Figure 7a is not likely the start of the growth phase. All types of electron and ion aurorae increase substantially at the substorm onset. So, the growth phase ends roughly at the same time for all electron and ion aurorae. In other words, the substorm onsets obtained from optical observations seem to agree with those obtained from the particle precipitation. The 1 hr and 15 min duration of the growth phase for the monoenergetic and broadband electron aurorae is at the upper end of the range of the growth phase obtained from ground magnetic field observations [e.g., *Bargatze et al*., 1999; *Huang et al*., 2003].

The end of the expansion phase can be defined as the time when the maximum power is reached. The duration of the diffuse aurora expansion phase is longer than that of the other two types of electron aurorae. The duration of the expansion phase of the diffuse aurora is 1 hr, whereas that of the monoenergetic and broadband aurorae is only about 15 min. It is interesting to note that the recovery phase onset for the electron diffuse aurora, ~1 hr after substorm onset, is comparable to the start of the plasma sheet recovery reported in *Baker et al*. [1994]. They reported that plasma sheet recoveries, e.g., expansion of plasma sheet, reduction of cross-tail current, etc., can occur with a delay ranging 10–120 min after substorm onset with a median delay of 45 min. However, their substorm onsets were determined from the ground magnetic field observations. The short expansion phase duration in the broadband aurora may result from the quick damping of the Alfvén waves as discussed in Section 3.

It is a challenge to determine the end of the recovery phase, primarily because it is hard to determine when the quiet time state is reached and what the quiet time power ought to be. For the broadband and monoenergetic electron aurorae, the powers at 3 hr after onset are approximately the same as those at 2 hr before onset. The declining power in the interval 2–1 hr before the substorm onset in the broadband and monoenergetic electron aurorae may suggest that some of the points in this interval come from the recovery phase of the preceding substorm. Assuming that (1) the minimum power before the substorm onset is the baseline for the quiet time power and (2) many points in the interval 2–1 hr before onset could also be in the interval 3–4 hr after onset, given our criterion for isolated substorms and so the durations of the monoenergetic and broadband electron aurora recovery phases can be estimated to be 3 hr and 30 min. It is harder to determine the recovery time for the diffuse electron aurora. Perhaps, some or many of the points in the interval 0 – 2 hr before onset may actually come from the recovery phase of the preceding substorm. This result may suggest that the recovery phase duration for the diffuse electron aurora could be more than 4 hr, but in order to get a better estimate, one would have to use substorms that are separated by more than 7 or 8 hr.

The recovery durations of all three types of the electron precipitation are larger than the 0.5–2 hr recovery duration obtained from the ground magnetic field observations [e.g., *Bargatze* *et al*., 1999; *McPherron et al*., 1986; *Baker et al*., 1981; *Huang et al*., 2003; *Horwitz*, 1985]. *Pulkkinen et al*. [1994] reported that the recovery period of the geosynchronous magnetic field and energetic particle observations is on the order of 1–3 hr. They attributed the long recovery of the near-Earth magnetic field to the effect of the developing ring current. However, it is not clear whether this can explain the long recovery period of the precipitating electrons, some of which map farther out than geosynchronous orbit.

Table 1 summarizes the time scales for the substorm cycles and phases for the three types of electrons.

8. The electron auroral dawn-dusk asymmetry modulations by substorms

Previous Sections present and discuss the electron energy fluxes for all three types of electron aurorae. The dawn-dusk asymmetries in diffuse and monoenergetic electron aurorae can be seen prominently in the electron energy fluxes in Figures 1, 2, and 5. In this section, we examine more quantitatively the dawn-dusk asymmetries and how these asymmetries are modulated by substorms.

Figure 8a plots the ratio of dawn (18:00 – 2400 MLT) to dusk (24:00 – 06:00 MLT) auroral power for monoenergetic (red), broadband (blue), and diffuse (green) electrons. The monoenergetic electron auroral power is larger at dawn than at dusk and this asymmetry, as measured by the dawn/dusk power ratio, increases after substorm onset. The asymmetry does not return to its growth phase value until ~135 min after onset. The increase of the asymmetry after the substorm onset may be related to the increase of Alfven wave activities at premidnight after onset as discussed in Sections 4 and 9.

The broadband electron auroral power does not show significant dawn-dusk asymmetry.

This can be seen by the dawn/dusk power ratio (blue line) that hovers around one in Figure 8a.

The diffuse electron auroral power has the opposite asymmetry from that of monoenergetic electron auroral power with the power at dawn larger than that at dusk (the dawn/dusk power ratio < 1). At 0 – 30 min after substorm onset, the dawn/dusk power ratio increases a bit, suggesting a smaller dawn-dusk asymmetry. This asymmetry can be seen more clearly in Figure 8b. The smaller dawn-dusk asymmetry after onset may be attributed to the plasma sheet electron injection and energization that occurs over a wide local time after onset, including at premidnight. The dawn/dusk power ratio minimum at –45 min before onset may be due to the interference from the long recovery phase of the preceding substorm (> 4 hr).

9. Is there any link between broadband and monoenergetic electrons?

As shown in Table 1 and Figures 7b and 7c, the substorm dynamics of broadband and monoenergetic electrons are more similar to each other than to those of diffuse electrons. For example, both broadband and monoenergetic electron powers peak 15 min after onset whereas diffuse electron power peaks 1 hr after onset. There may be a link between the mechanisms for broadband and monoenergetic electrons.

Substorms increase the Alfvén wave activities in the magnetotail [e.g., *Lessard et al.*, 2006]. The high frequency Alfvén wave interaction with electrons lead to time-varying parallel electric fields that accelerate electrons, resulting in the broadband signature in the electrons [*Chaston et al.*, 2002; 2003; 2008]. This is consistent with the broadband electron energy flux increase after substorm onset around 21:00 – 02:00 MLT, as shown in Figure 7b. However, Alfvén waves can also be responsible for the monoenergetic electrons. For example, *Hull et al.* [2010] suggests that the Alfvén waves can lead to the formation of density cavities and quasi-static parallel electric fields. The low frequency Alfvén waves can accelerate electrons that lead to the monoenergetic signature [*Damiano and Johnson*, 2012; *Pritchett and Coroniti*, 2010]. After a few Alfvén bounce periods, the Alfvén waves damp due to electron energy absorption and/or Joule dissipation [*Hull et al.*, 2010; *Lysak and Song*, 2003; *Damiano and Johnson*, 2012]. As a result, the broadband auroral electron power decays after a few Alfvén bounce periods (~ 15 min), as seen in Figure 7b. On the other hand, the low frequency Alfvén waves damp more slowly, which is consistent with the slower decay of the monoenergetic electron power seen in Figure 7c. The decay time scales can be illustrated with the time it takes the power to reach its half maximum value from the maximum value at the end of the expansion phase. As can be seen in Figure 7 and summarized in Table 1, the time it takes to reach half maximum is ~1.6 hr for the monoenergetic electrons, but only ~0.42 hr for broadband electrons.

Figure 7b shows that after reaching its maximum value, the broadband electron power initially decays rapidly and then slowly. This two stage decay of the broadband electron power suggests that after the rapid decay of the main Alfvén waves in the interval 15–45 min after onset, there seems to be residual Alfvén waves that slowly decay that can be seen at approximately 45 min after onset. These residual Alfvén waves seem to linger on for the rest of the recovery period, which has the same time scale as the recovery period for the monoenergetic electrons.

However, a significant amount of monoenergetic electrons are likely produced by quasi-static electric fields that can be attributed to mechanisms other than low frequency Alfvén waves. For example, in upward field-aligned current regions, quasi-static electric fields can arise when the magnetospheric electron density is too low to carry the currents [*Knight*, 1973]. Figures 3 and 5 show that monoenergetic and broadband electrons are not always observed in the same region. They seem to overlap roughly in the region spanning 21:00–01:00 MLT. Westward of the overlapping region, e.g., MLT < 21:00, monoenergetic electrons can be observed without significant broadband electrons.

10. Summary

Substorms change the magnetospheric configuration, e.g., when the magnetic field lines change from stretched tail-like to more dipolar configurations. During this process, a significant amount of energy is released, some of which energizes precipitating particles. On the nightside, ion and all three types of electron (diffuse, monoenergetic, and broadband) energy fluxes and powers increase at or shortly after substorm onset. However, the energy increases differ for each type of aurora. The increases are 71%, 170%, and 310% for the monoenergetic, broadband, and diffuse electron auroral powers, respectively. In contrast, the ion pressure increases only by 30% [Wing et al., 2013]. At the end of the expansion phase (maximum power), different types of electron auroral power decays at different rates. The time it takes to reach half maximum power from the maximum for the broadband, diffuse, and monoenergetic electrons are ~0.42, ~1.2, and ~1.6 hr, respectively. Among the electron aurorae, the broadband aurora has the smallest power, followed by the monoenergetic aurora, whereas the diffuse aurora has the largest power. The ion auroral power and energy flux are comparable to those of the broadband electron aurora during the growth phase, but after the onset the broadband electron auroral power and energy fluxes increase much more than those of the ion aurora. Relative to their pre onset values, substorms appear to energize ion aurora less than electron aurora of any kind.

The MLT distribution of each type of aurora also differs. The diffuse electrons and auroral power concentrate mainly in 22:00–09:00 MLT, which overlap much with the whistler-mode chorus waves that can pitch-angle scatter magnetospheric electrons into the loss cone. However, the monoenergetic auroral power mainly from the dusk-midnight sector, 18:00-24:00 MLT, whereas the broadband auroral power comes mainly from the region centered at premidnight, spanning roughly 21:00 to 02:00 MLT. The broadband electrons result from time varying electric fields due to electron-Alfvén wave interaction. On the other hand, the monoenergetic electrons are magnetospheric electrons that have gone through quasi-static parallel electric field in the upward field-aligned current regions. However, there may be a connection between the mechanism for monoenergetic and broadband electrons – low frequency Alfvén wave-electron interaction can lead to monoenergetic electron signature.

After substorm onset, the dawn-dusk asymmetry increases for about 135 min in the monoenergetic electron power. In contrast, after the onset, the dawn-dusk asymmetry decreases for about 30 min in the diffuse electron power. In comparison, substorms do not change the dawn-dusk asymmetry of the broadband electron power by much.

Near the end of the growth phase, i.e., $\Delta t = -30$ to -15 min, the ion energy flux peaks at 18:00–21:00 MLT sector, which can be attributed to the ion curvature and gradient westward drifts toward dusk. There is also a second peak at 02:00–05:00 MLT, which can be attributed to cold solar wind ion entry along the dawn flank, flow stagnation, and enhanced $\mathbf{E} \times \mathbf{B}$.

The substorm cycle time scales for electron precipitation are longer than those previously reported for other magnetospheric and ionospheric parameters. The substorm complete cycle duration for monoenergetic and broadband electrons is ~ 5hr, but it is greater than 5 hr for diffuse electrons.

Acknowledgments. Gordon Wilson and Air Force Research Lab have been helpful in acquisition of DMSP SSJ/4/5 data, as has the World Data Center in Boulder, Colorado. Simon Wing gratefully acknowledges support from NSF Grant AGS-1058456 and NASA Grants (NNX13AE12G, NNX15AJ01G). Jay R. Johnson acknowledges support from NASA Grants (NNH11AR07I, NNX14AM27G, NNH14AY20I), NSF Grants (ATM0902730, AGS-1203299), and DOE contract DE-AC02-09CH11466.

References

Angelopoulos et al. (2008), Tail reconnection triggering substorm onset, Science, 321(5891), 931-935, DOI: 10.1126/science.1160495.

Baker, D. N., E. W. Hones, Jr., P. R. Higbie, and R. D. Belian (1981), Global properties of the magnetosphere during a substorm growth phase: A case study, J. *Geophys. Res*., 86, 8941–8956.

Baker, D. N., T. I. Pulkkinen, E. W. Hones Jr., R. D. Belian, R. L. McPherron, and V. Angelopoulos (1994), Signatures of the substorm recovery phase at high-altitude spacecraft, *J. Geophys. Res*., 99, 10,967-10,979.

Bargatze, L. F., T. Ogino, R. L. McPherron, and R. J. Walker (1999), Solar wind magnetic field control of magnetospheric response delay and expansion phase onset timing, J. Geophys. Res., 104, 14,583-14,599.

Baumjohann, W., M. Hesse, S. Kokubun, T. Mukai, T. Nagai, and A. A. Petrukovich (1999), Substorm dipolarization and recovery, *J. Geophys. Res.*, 104(A11), 24,995–25,000, doi:10.1029/1999JA900282.

Birn, J., and E. W. Hones Jr. (1981), Three-dimensional computer modeling of dynamic reconnection in the geomagnetic tail, *J. Geophys. Res.*, *86*, 6802–6808, doi:10.1029/JA086iA08p06802.

Birn, J., M. Hesse, K. Schindler, and S. Zaharia (2009), Role of entropy in magnetotail dynamics, *J. Geophys. Res*., 114, A00D03, doi:10.1029/2008JA014015.

Birn, J., R. Nakamura, E. V. Panov, and M. Hesse (2011), Bursty bulk flows and dipolarization in MHD simulations of magnetotail reconnection, J. Geophys. Res., 116, A01210, doi:10.1029/2010JA016083.

Camporeale, E., G. L. Delzanno, and P. Colestock (2012), Lower hybrid to whistler mode conversion on a density striation, J. Geophys. Res., 117, A10315, doi:10.1029/2012JA017726.

Camporeale, E. (2015), Resonant and nonresonant whistlers-particle interaction in the radiation belts. Geophys. Res. Lett., 42, 3114–3121. doi: 10.1002/2015GL063874.

Camporeale, E., & Zimbardo, G. (2015). Wave-particle interactions with parallel whistler waves: nonlinear and time-dependent effects revealed by Particle-in-Cell simulations, Phys. Plasmas 22, 092104, doi.org/10.1063/1.4929853.

Chaston, C., et al. (2008), Turbulent heating and cross-field transport near the magnetopause from THEMIS, *Geophys. Res. Lett.*, 35, L17S08, doi:10.1029/2008GL033601.

Chaston, C. C., C. W. Carlson, J. P. McFadden, R. E. Ergun, and R. J. Strangeway (2007), How important are dispersive Alfvén waves for auroral particle acceleration?, *Geophys. Res. Lett.*, 34, L07101, doi:10.1029/2006JG029144.

Chaston, C. C., J. W. Bonnell, C. W. Carlson, J. P. McFadden, R. E. Ergun, and R. J. Strangeway (2003), Properties of small-scale Alfvén waves and accelerated electrons from FAST, *J. Geophys. Res.*, 108, 8003, doi:10.1029/2002JA009420.

Chaston, C. C., J. W. Bonnell, L. M. Peticolas, C. W. Carlson, J. P. McFadden, and R. E. Ergun (2002), Driven Alfvén waves and electron acceleration, *Geophys. Res. Lett.*, 29, 1535.

Christon, S. P., D. J. Williams, D. G. Mitchell, C. Y. Huang, and L. A. Frank (1991), Spectral Characteristics of Plasma Sheet Ion and Electron Populations during Disturbed Geomagnetic Conditions, *J. Geophys. Res.*, 96(A1), 1–22, doi:10.1029/90JA01633.

Damiano, P. A., A. N. Wright, R. D. Sydora, and J. C. Samson (2007), Energy dissipation via electron energization in standing shear Alfvén waves, Phys. Plasmas, 14, 062,904.

Damiano, P. A., and J. R. Johnson (2012), Electron acceleration in a geomagnetic Field Line Resonance, *Geophys. Res. Lett.*, 39, L02102, doi:10.1029/2011GL050264.

Damiano, P. A., J. R. Johnson, and C. C. Chaston (2015), Ion temperature effects on magnetotail Alfvén wave propagation and electron energization, *J. Geophys. Res.*, 120, 5623–5632, doi:10.1002/2015JA021074.

Frey, H. U., S. B. Mende, V. Angelopoulos, and E. F. Donovan (2004), Substorm onset observations by IMAGE-FUV, *J. Geophys. Res., 109,* A10304, doi:10.1029/2004JA010607.

Friedel, R. H. W., H. Korth, M. G. Henderson, and M. F. Thomsen (2001), Plasma sheet access to the inner magnetosphere, *J. Geophys. Res.*, *106*, 5845-5858.

Haerendel, G. (2010), Equatorward moving arcs and substorm onset, J. Geophys. Res., 115, A07212, doi:10.1029/2009JA015117.

Hasegawa, A., Particle acceleration by MHD surface wave and formation of the aurora, *J. Geophys. Res.*, *81*, 5083, 1976.

Hodges, J. L., Jr., and E. L. Lehmann (1967), *J. Am. Stat. Ass*., 62, 319, 926–931.

Horne, R. B., and R. M. Thorne (2003), Relativistic electron acceleration and precipitation during resonant interactions with whistler-mode chorus, Geophys. Res. Lett., 30, 1527, doi:10.1029/2003GL016973, 10.

Horwitz, J. L. (1985), The substorm as an internal magnetospheric instability: Substorms and their characteristic time scales during intervals of steady interplanetary magnetic field, J. Geophys. Res., 90, 4164–4170.

Huang, C.-S., G. D. Reeves, J. E. Borovsky, R. M. Skoug, Z. Y. Pu, and G. Le (2003), Periodic magnetospheric substorms and their relationship with solar wind variation, J. Geophys.

Res., 108(A6), 1255, doi:10.1029/2002JA009704.

Hull, A. J., M. Wilber, C. C. Chaston, J. W. Bonnell, J. P. McFadden, F. S. Mozer, M. Fillingim, and M. L. Goldstein (2010), Time development of field-aligned currents, potential drops, and plasma associated with an auroral poleward boundary intensification, J. Geophys. Res., 115, A06211, doi:10.1029/2009JA014651.

Hsu, T.-S., and R. L. McPherron (2004), Average characteristics of triggered and nontriggered substorms, *J. Geophys. Res.*, *109*, A07208, doi:10.1029/2003JA009933.

Johnson, J. R., and S. Wing (2009), Northward interplanetary magnetic field plasma sheet entropies, J. Geophys. Res., 114, A00D08, doi:10.1029/2008JA014017.

Johnson, J. R., and S. Wing (2014), External versus internal triggering of substorms: An information-theoretical approach, Geophys. Res. Lett., 41, 5748–5754, doi:10.1002/2014GL060928.

Jordanova, V. K., C. J. Farrugia, R. M. Thorne, G. V. Khazanov, G. D. Reeves, and M. F. Thomsen (2001), Modeling ring current proton precipitation by electromagnetic ion cyclotron waves during the May 14–16, 1997, storm, *J. Geophys. Res.*, 106(A1), 7–22, doi:10.1029/2000JA002008.

Kan, J. R., D. U. Longenecker, and J. V. Olson (1982), A transient response model of Pi 2 pulsations, *J. Geophys. Res.*, 87(A9), 7483–7488, doi:10.1029/JA087iA09p07483.

Keiling, A., J. R. Wygant, C. Cattell, W. Peria, G. Parks, M. Temerin, F. S. Mozer, C. T. Russell, and C. A. Kletzing (2002), Correlation of Alfvén wave Poynting flux in the plasma sheet at 4–7 *RE* with ionospheric electron energy flux, *J. Geophys. Res.*, *107*, 1132, doi:10.1029/2001JA900140.

Keiling, A., J. R. Wygant, C. A. Cattell, F. S. Mozer, and C. T. Russell (2003), The global morphology of wave Poynting flux: Powering the aurora, Science, 299, 383-386, DOI: 10.1126/science.1080073.

Kenney, J. F., and E. S. Keeping (1951), Mathematics of Statistics part two, 2nd edition, pp. 370–371, D. V. Nostrand Co. Inc., Princeton, NJ, USA.

Kletzing, C. A. (1994), Electron Acceleration by Kinetic Alfvén Waves, *J. Geophys. Res.*, *99*(A6), 11,095–11,103, doi:10.1029/94JA00345.

Kletzing, C. A., J. D. Scudder, E. E. Dors, and C. Curto (2003), The auroral source region: plasma properties of the high altitude plasma sheet, *J. Geophys. Res., 108,* 1360, doi:10.1029/2002JA009678.

Knight, L. (1973), Parallel electric fields, *Planet. Space Sci*., 21, 741-750.

Korth, H., M. F. Thomsen, J. E. Borovsky, and D. J. McComas (1999), Plasma sheet access to geosynchronous orbit, *J. Geophys. Res., 104*, 25,047-25,061.

Lessard, M. R., E. J. Lund, S. L. Jones, R. L. Arnoldy, J. L. Posch, M. J. Engebretson, and K. Hayashi (2006), Nature of Pi1B pulsations as inferred from ground and satellite observations, *Geophys. Res. Lett., 33,* L14108, doi:10.1029/2006GL026411.

Li, W., Y. Y. Shprits, and R. M. Thorne (2007), Dynamic evolution of energetic outer zone electrons due to wave-particle interactions during storms, J. Geophys. Res., 112, A10220, doi:10.1029/2007JA012368.

Liou, K., P. T. Newell, C.-I. Meng (1997), A. T. Y. Lui, M. Brittnacher, and G. Parks, Dayside auroral activity as a possible precursor of substorm onsets: a survey using POLAR UVI imagery, *J. Geophys. Res., 102,* 19835-19844.

Liou, K., P. T. Newell, D. G. Sibeck, C.-I. Meng, M. Brittnacher, and G. Parks (2001), Observation of IMF and seasonal effects in the location of auroral substorm onset, *J.*

Geophys. Res., 106, 5799.

Lui, A. (1994), Mechanisms for the substorm current wedge, in Substorms 2: Proceedings of the Second International Conference on Substorms, Fairbanks, Alaska, March 7–11, 1994, edited by J. R. Kan, J. D. Crave, and S.-I. Akasofu, pp. 195–203, Univ. of Alaska, Fairbanks, Alaska.

Lui, A. T. Y. (1991), Extended consideration of a synthesis model for magnetospheric substorms, in *Magnetospheric Substorms*, pp. 43-60, *Geophys. Monog.*, *64*, edited by J. R. Kan, T. A. Potemra, S. Kokubun, and T. Ijima, AGU, Washington D.C.,

Lui, A. T. Y. (2004), Potential plasma instabilities for substorm expansion onsets, Space Sci. Rev., 113, 127 – 206, doi:10.1023/B:SPAC. 0000042942.00362.4e.

Lyons, L. R. and T. W. Speiser (1982), Evidence for current sheet acceleration in the geomagnetic tail, *J. Geophys. Res.*, 87(A4), 2276–2286, doi:10.1029/JA087iA04p02276.

Lyons, L. R., G. T. Blanchard, J. C. Samson, R. P. Lepping, T. Yamamoto, and T. Moretto (1997), Coordinated observations demonstrating external substorm triggering, *J. Geophys. Res.*, *102*, 27,039–27,052, doi:10.1029/97JA02639.

Lysak, R. L., and Y. Song (2003), Kinetic theory of the Alfvén wave acceleration of auroral electrons, *J. Geophys. Res.*, 108, 8005, doi:10.1029/2002JA009406.

Lysak, R. L., and Y. Song (2011), Development of parallel electric fields at the plasma sheet boundary layer, *J. Geophys. Res.*, *116*, A00K14, doi:10.1029/2010JA016424, [printed 117(A1), 2012].

McPherron, R. L. (1972), Substorm related changes in the geomagnetic tail: The growth phase, Planet. Spa. Sci., 29, 1521–1539.

McPherron, R. L., T.-S. Hsu, J. Kissinger, X. Chu, and V. Angelopoulos (2011), Characteristics of plasma flows at the inner edge of the plasma sheet, *J. Geophys. Res*., 116, A00133, doi:10.1029/2010JA015923.

McPherron, R. L., T. Terasawa, and A. Nishida (1986), Solar wind triggering of substorm expansion onset, *J. Geomag. Geoelectr*, 38, 1089–1108.

McPherron, R. (1991), Physical processes producing magnetospheric substorms and magnetic storms, in *Geomagnetism*, edited by J. Jacobs, pp. 593–739, Academic Press, London, U. K.

Meng, C.-I., and K. Liou (2004), Substorm timings and time scales: A new aspect, Space Sci. Rev., 113, 41 – 75, doi:10.1023/B:SPAC.0000042939.88548.68.

Nakamura, R., W. Baumjohann, M. Brittmacher, V. A. Sergeev, M. Kubyshkina, T. Mukai, and K. Liou (2001), Flow bursts and auroral activations, *J. Geophys. Res*., 106(A6), 10,777–10,789.

Newell, P. T., A. R. Lee, K. Liou, S.-I. Ohtani, T. Sotirelis, and S. Wing (2010), Substorm cycle dependence of various types of aurora, *J. Geophys. Res.*, 115, A09226, doi:10.1029/2010JA015331.

Newell, P. T., T. Sotirelis, and S. Wing (2009), Diffuse, monoenergetic, and broadband aurora: the global precipitation budget, *J. Geophys. Res., 114*, A09207, doi:10.1029/2009JA014326.

Ni, B., R. M. Thorne, N. P. Meredith, R. B. Horne, and Y. Y. Shprits (2011), Resonant scattering of plasma sheet electrons leading to diffuse auroral precipitation: 2. Evaluation for whistler mode chorus waves, J. Geophys. Res., 116, A04219, doi:10.1029/2010JA016233.

Ni, B., R. M. Thorne, Y. Y. Shprits, and J. Bortnik (2008), Resonant scattering of plasma sheet electrons by whistler-mode chorus: Contribution to diffuse auroral precipitation, Geophys.

Res. Lett., 35, L11106, doi:10.1029/2008GL034032.

Nishida, A. (1979), Possible origin of transient dusk-to-dawn electric field in the nightside magnetosphere, *J. Geophys. Res.*, 84(A7), 3409–3412, doi:10.1029/JA084iA07p03409.

Pritchett, P. L., and F. V. Coroniti (2010), A kinetic ballooning/interchange instability in the magnetotail, *J. Geophys. Res.*, 115, A06301, doi:10.1029/2009JA014752.

Pulkkinen, T. I., D. N. Baker, P. K. Toivanen, R. J. Pellinen, R. H. W. Friedel, and A. Korth (1994), Magnetospheric field and current distributions during the substorm recovery phase, *J. Geophys. Res*., 99, 10,955-10,966.

Reeves, G. D., A. Chan, and C. Rodger (2009), New Directions for Radiation Belt Research, *Space Weather*, 7, S07004, doi:10.1029/2008SW000436.

Rostoker, G. (2002), Identification of substorm expansive phase onsets, J. Geophys. Res. Lett.,107(A7), doi:10.1029/2001JA003504.

Schekochihin, A. A., S. C. Cowley, W. Dorland, G. W. Hammett, G. G. Howes, E. Quataert, and T. Tatsuno (2009), Astrophysical Gyrokinetics: Kinetic and Fluid Turbulent Cascades in Magnetized Weakly Collisional Plasmas, *Astrophysical Journal Supplemental Series*, 182, 310-377, doi:10.1088/0067-0049/182/1/310.

Sergeev, V.A., K. Liou, P. T. Newell, S.-I. Ohtani, M. R. Hairston, and F. Rich (2004), Auroral streamers: Characteristics of associated precipitation, convection and field-aligned currents, *Ann. Geophys*., 22, 537–548.

Sergeev, V. A., M. Malkov, and K. Mursula (1993), Testing the isotropic boundary algorithm method to evaluate the magnetic field configuration in the tail, *J. Geophys. Res*., *98*, 7609-7620.

Sergeev, V. A., E. M. Sazhina, N. A. Tsyganenko, J. A. Lundblad and F. Soraas (1983), Pitch-angle scattering of energetic protons in the magnetotail current sheet as the dominant source of their isotropic precipitation into the nightside ionosphere, *Planet. Space Sci*., 31, 1147–1155.

Sergeev, V. A., V. Angelopoulos, and R. Nakamura (2012), Recent advances in understanding substorm dynamics, Geophys. Res. Lett., 39, L05101, doi:10.1029/2012GL050859

Sergeev, V. A., S. A. Chernyaeva, S. V. Apatenkov, N. Y. Ganushkina, and S. V. Dubyagin (2015), Energy–latitude dispersion patterns near the isotropy boundaries of energetic protons, Ann. Geophys., 33, 1059-1070, doi:10.5194/angeo-33-1059-2015.

Spence, H. E., and M. G. Kivelson (1993), Contributions of the low-latitude boundary layer to the finite width magnetotail convection model, J. Geophys. Res., 98(A9), 15487–15496, doi:10.1029/93JA01531.

Speiser, T. W. (1965), Particle trajectories in model current sheets: 1. Analytical solutions, *J. Geophys. Res.*, 70(17), 4219–4226, doi:10.1029/JZ070i017p04219.

Stasiewicz, K., P. Bellan, C. Chaston, C. Kletzing, R. Lysak, J. Maggs, O. Pokhotelov, C. Seyler, P. Shukla, L. Stenflo, A. Streltsov, and J. E. Wahlund (2000), Small scale Alfvénic structure in the aurora, *Space Science Rev., 92,* 423.

Summers, D., R. M. Thorne, and F. Xiao (1998), Relativistic theory of wave-particle resonant diffusion with application to electron acceleration in the magnetosphere, *J. Geophys. Res.*, 103(A9), 20,487–20,500, doi:10.1029/98JA01740.

Tanskanen, E., T. I. Pulkkinen, and H. E. J. Koskinen (2002), Substorm energy budget during low and high solar activity: 1997 and 1999 compared, *J. Geophys. Res*., 107(A6), 1086, 10.1029/2001JA900153.

Thorne, R. M. (2010), Radiation belt dynamics: The importance of wave-particle interactions, *Geophys. Res. Lett*., 37, L22107, doi:10.1029/2010GL044990.

Tsyganenko, N. A., and D. G. Sibeck (1994), Concerning Flux Erosion from the Dayside Magnetosphere, *J. Geophys. Res.*, 99(A7), 13,425–13,436, doi:10.1029/94JA00719.

Tsyganenko, N. A., D. P. Stern, and Z. Kaymaz (1993), Birkeland Currents in the Plasma Sheet, *J. Geophys. Res.*, 98(A11), 19,455–19,464, doi:10.1029/93JA01922.

Vasconez, C. L., Valentini, F., Camporeale, E., & Veltri, P. (2014). Vlasov simulations of kinetic Alfvén waves at proton kinetic scales. *Phys. Plasmas* , *21*(11), 112107.

Wang, C.-P., L. R. Lyons, M. W. Chen, and R. A. Wolf (2001), Modeling the quiet time inner plasma sheet protons, J. Geophys. Res., 106(A4), 6161–6178, doi:10.1029/2000JA000377.

Wang, C-P, L. R. Lyons, M. W. Chen, R. A. Wolf, and F. R. Toffoletto (2003), Modeling the inner plasma sheet protons and magnetic field under enhanced convection, *J. Geophys. Res*., *108* (A2), 1074, doi:10.1029/2002JA0009620.

Wang, C.-P., L. R. Lyons, M. W. Chen, and F. R. Toffoletto (2004), Modeling the transition of the inner plasma sheet from weak to enhanced convection, J. Geophys. Res., 109, A12202, doi:10.1029/2004JA010591.

Wang, C.-P., L. R. Lyons, J. M. Weygand, T. Nagai, and R. W. McEntire (2006), Equatorial distributions of the plasma sheet ions, their electric and magnetic drifts, and magnetic fields under different interplanetary magnetic field B_z *conditions, J. Geophys. Res., 111, A04215, doi:10.1029/2005JA011545.*

Wang, C.-P., M. Gkioulidou, L. R. Lyons, R. A. Wolf, V. Angelopoulos, T. Nagai, J. M. Weygand, and A. T. Y. Lui (2011), Spatial distributions of ions and electrons from the plasma sheet to the inner magnetosphere: Comparisons between THEMIS-Geotail statistical results and the Rice convection model, J. Geophys. Res., 116, A11216, doi:10.1029/2011JA016809.

Watanabe, M., and T. Iijima (1993), Substorm Growth Phase on the Magnetotail, *J. Geophys. Res.*, 98(A10), 17,299–17,316, doi:10.1029/93JA01474.

Watt, C. E. J., and R. Rankin (2009), Electron trapping in shear Alfvén waves that power the aurora, *Phys. Rev. Lett.*, 102, 045002.

Watt, C. E. J., R. Rankin, I. J. Rae, and D. M. Wright (2005), Self-consistent electron acceleration due to inertial Alfvén wave pulses, *J. Geophys. Res.*, 110, A10S07, doi:10.1029/2004JA010877.

Wing, S., M. Gkioulidou, J. R. Johnson, P. T. Newell, and C.-P. Wang (2013), Auroral particle precipitation characterized by the substorm cycle, J. Geophys. Res. Space Physics, 118,1022–1039, doi:10.1002/jgra.50160.

Wing, S., and J. R. Johnson (2010), Introduction to special section on Entropy Properties and Constraints Related to Space Plasma Transport, *J. Geophys. Res.*, 115, A00D00, doi:10.1029/2009JA014911.

Wing, S., and J. R. Johnson (2009), Substorm entropies, *J. Geophys. Res.*, 114, A00D07, doi:10.1029/2008JA013989.

Wing, S., and D. G. Sibeck (1997), The effects of interplanetary magnetic field Z-component and the solar wind dynamic pressure on the magnetospheric magnetic field line, *J. Geophys. Res.*, 102, 7207–7216.

Wing, S., J. W. Gjerloev, J. R. Johnson, and R. A. Hoffman (2007), Substorm plasma sheet ion pressure profiles, *Geophys. Res. Lett.*, 34, L16110, doi:10.1029/2007GL030453.

Wing, S., J. R. Johnson, P. T. Newell, and C.-I. Meng (2005), Dawn-dusk asymmetry in the northward IMF plasma sheet, *J. Geophys. Res.*, 110, A08205, doi:10.1029/2005JA011086.

Wing, S., and P. T. Newell (2002), 2D plasma sheet density profile for northward and southward

IMF, *Geophys. Res. Lett.*, 29(9), 10.1029/2001GL013950.

Wing, S., and P. T. Newell (1998), Central plasma sheet ion properties as inferred from ionospheric observations, *J. Geophys. Res.*, 103, 6785–6800.

Wolf, R. A., Wan, X. Xing, J. Zhang, and S. Sazykin (2009), Entropy and plasma sheet transport, *J. Geophys. Res.*, 114, A00D05, doi:10.1029/2009JA014044.

Wygant, J. R., et al. (2002), Evidence for kinetic Alfvén waves and parallel electron energization at 4–6 *RE* altitudes in the plasma sheet boundary layer, *J. Geophys. Res.*, *107*, 1201, doi:10.1029/2001JA900113.

Zanetti, L. J., and T. Potemra (1986), The relationship of Birkeland and ionospheric current systems to the interplanetary magnetic field, in *Solar Wind-Magnetosphere Coupling*, edited by Y. Kamide and J. A. Slavin, pp. 547–562, Terra Sci., Tokyo.

Zhang, J.-C., R. A. Wolf, S. Sazykin, and F. R. Toffoletto (2008), Injection of a bubble into the inner magnetosphere, *Geophys. Res. Lett.*, 35, L02110, doi:10.1029/2007GL032048.

Table

	total substorm cycle	growth phase	expansion phase	recovery phase	Δt at half max
diffuse electrons	> 5hr	?	1 hr	>4 hr?	~1.2 hr
broadband electrons	~ 5 hr	1.25 hr	0.25 hr	~3.50 hr	~0.42 hr
monoenergetic electrons	~ 5 hr	1.25 hr	0.25 hr	~3.50 hr	~1.6 hr

Table 1. Summary of the time scales of the substorm cycles and phases from electron precipitation perspective. The growth and recovery phases for the diffuse electrons are hard to determine (see text). Δt at half max denotes the time it takes to reach half maximum (green asterisks in Figure 7) from the maximum auroral power at end of the expansion phase, which gives a measure of how quickly the auroral power decays after reaching the maximum value.

Figures

Diffuse auroral electron energy flux

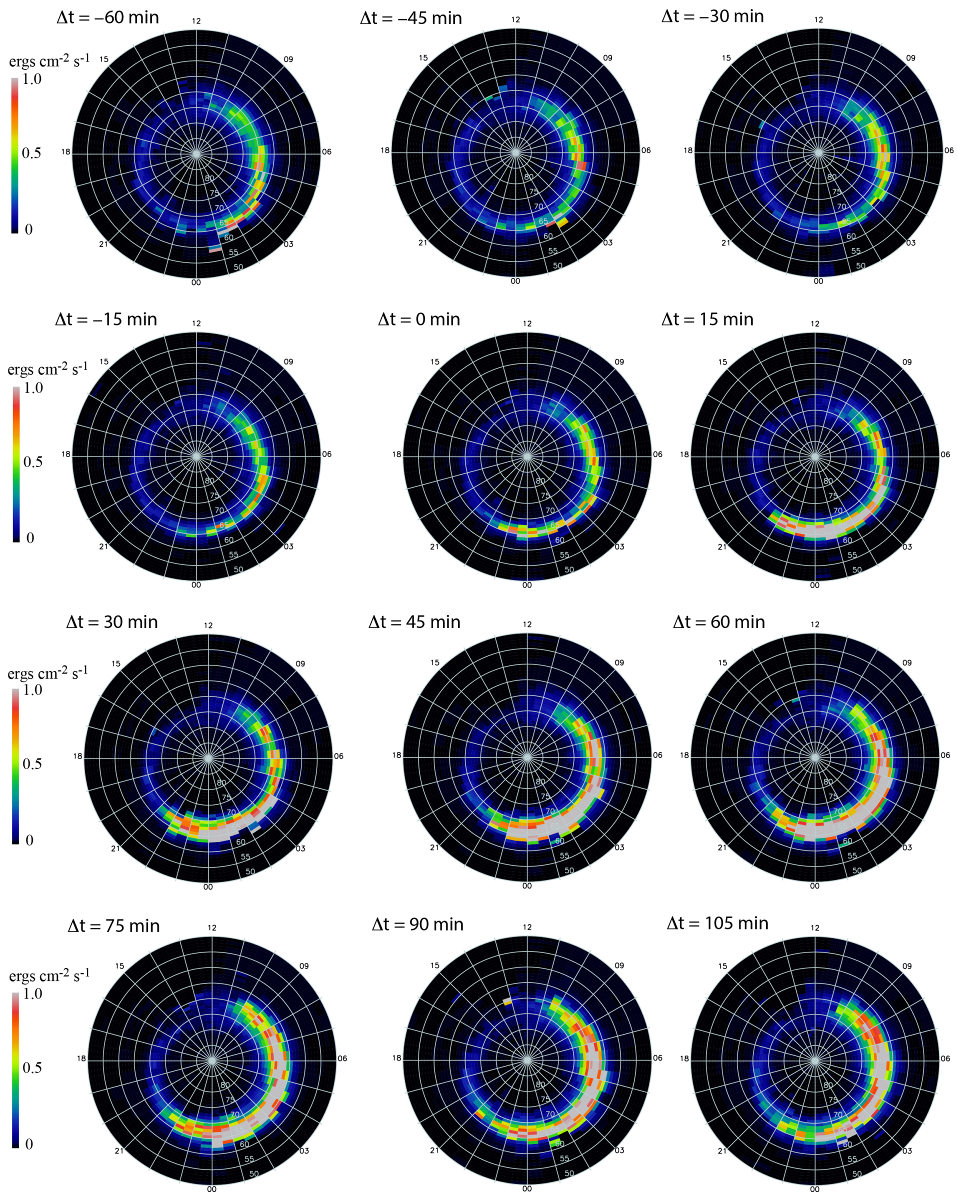

Figure 1. Diffuse auroral electron energy flux from 1 hr before to 1 hr and 45 min after the substorm onset. Each map shows the median energy flux of 48 MLT by 40 MLat bins at15 min time steps centered at the time labeled. The substorm onset occurs at Δt = 0 min. The MLat range is 50°–90°, with data from the two hemispheres combined. (from Wing et al. [2013]). 1677 substorm events were considered for the construction of this and other figures in this paper.

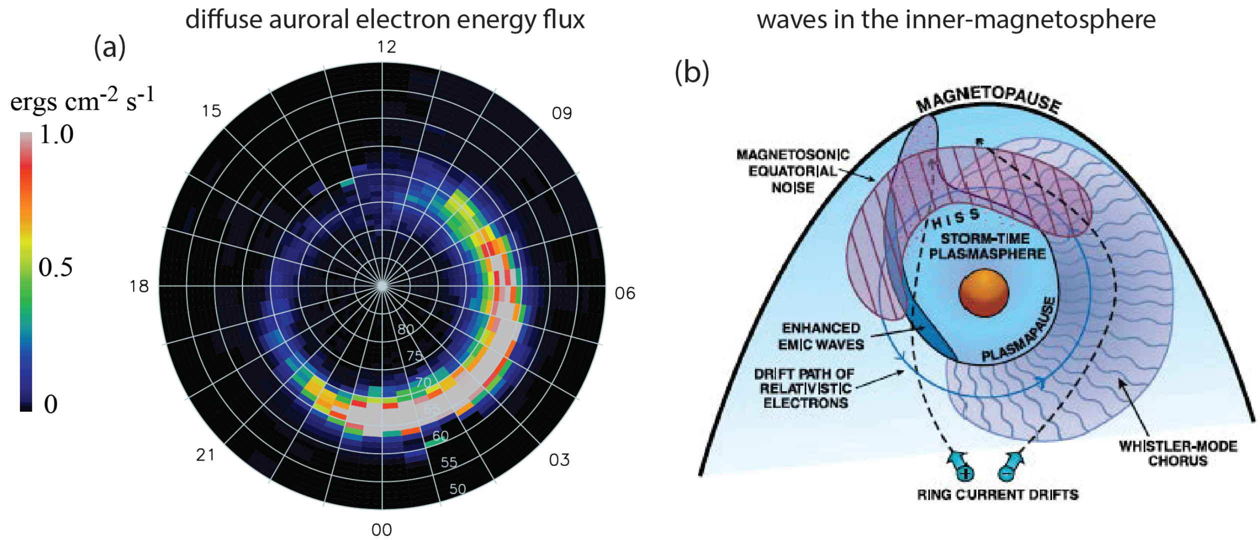

Figure 2. Diffuse auroral electron spatial distribution is similar to that of whistler-mode chorus waves. (a) diffuse auroral electron energy flux 60 min after substorm onset (from Figure 1). (b) Schematic showing spatial distribution of important waves in the inner magnetosphere (from Thorne [2010]).

Broadband auroral electron energy flux

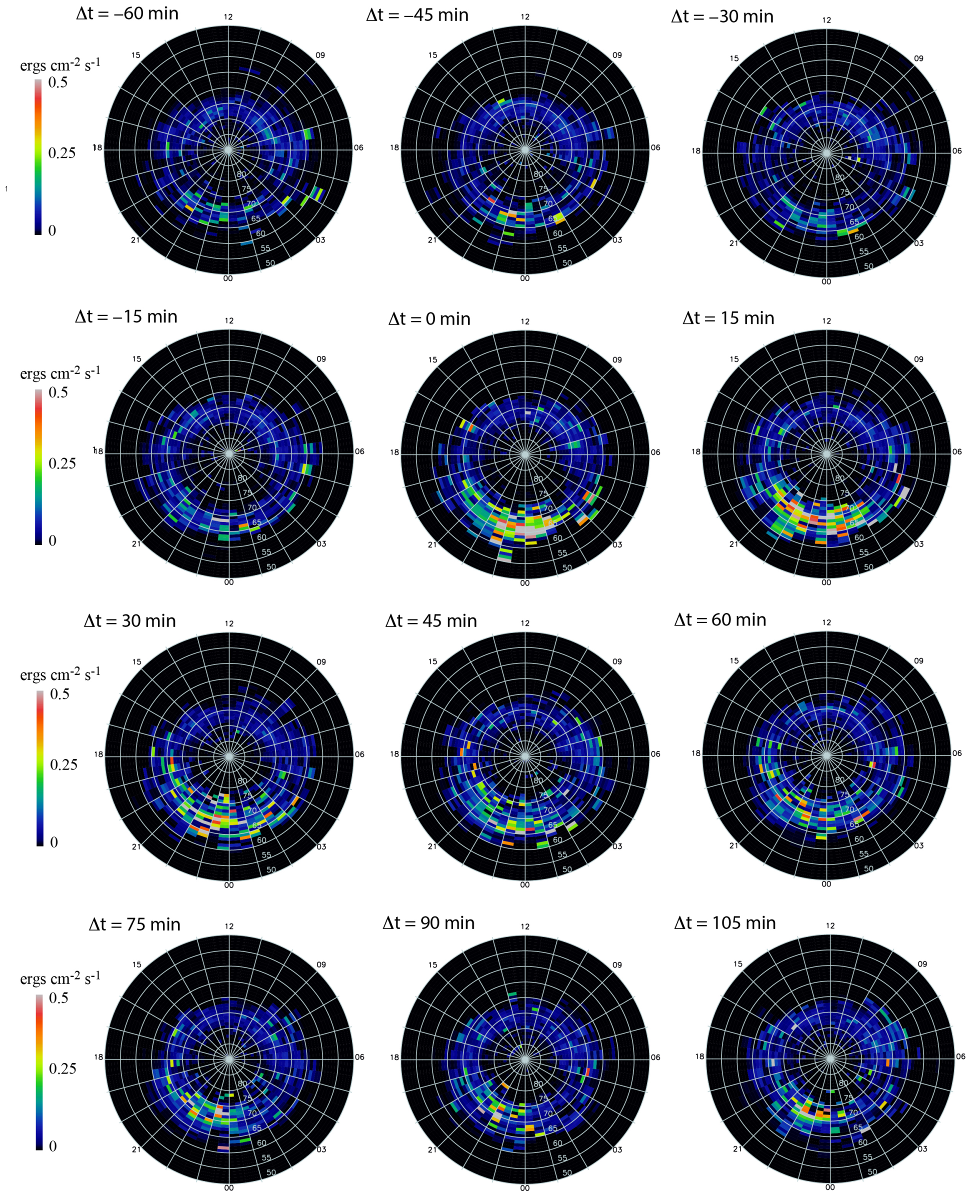

Figure 3. Broadband auroral electron energy flux from 1 hr before to 1 hr and 45 min after the substorm onset in the same format as in Figure 1. The substorm onset occurs at Δt = 0 min. (from Wing et al. [2013])

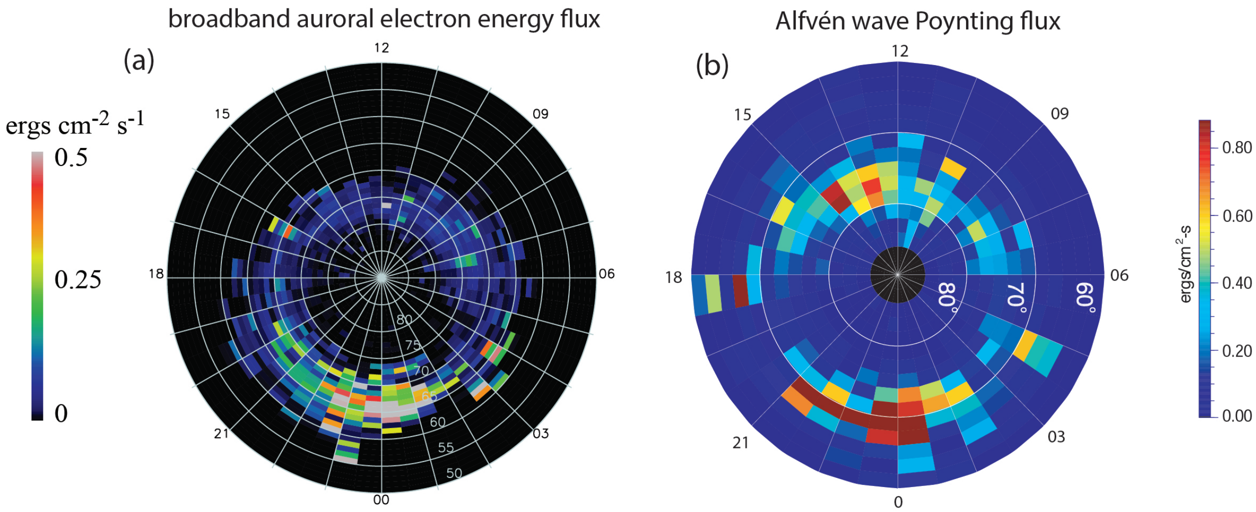

Figure 4. Broadband auroral electrons have similar spatial distribution with that of Alfvén waves in the magnetosphere. (a) Broadband auroral electron energy flux near substorm onset (from Figure 3). (b) Average Alfvén wave Poynting flux flowing toward the Earth at high-altitude as observed by Polar satellite at 25,000 to 38,000 km obtained from an interval when large Alfvén waves were present during auroral and substorm activity (from Keiling et al. [2003]).

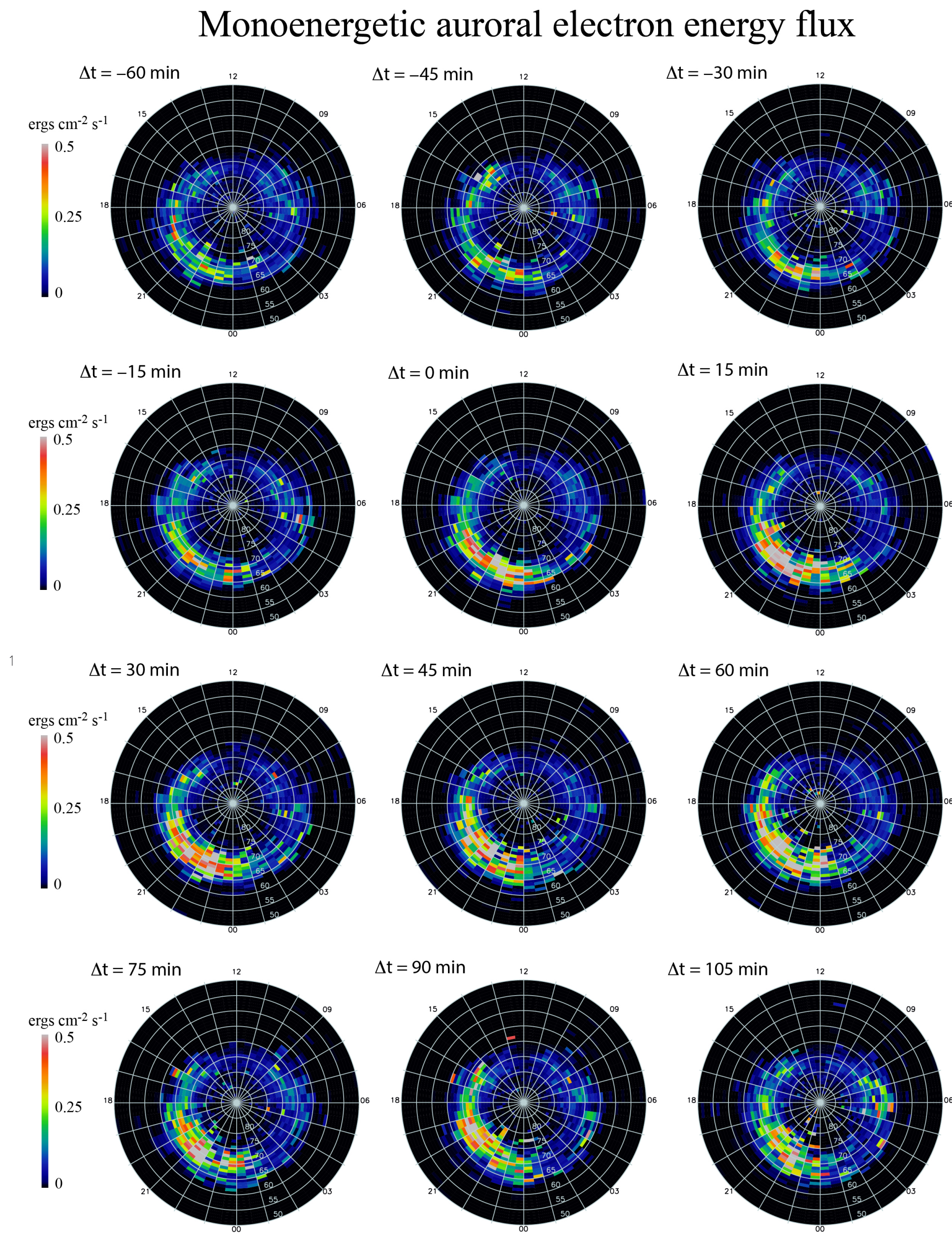

Figure 5. Monoenergetic auroral electron energy flux from 1 hr before to 1 hr and 45 min after the substorm onset in the same format as in Figure 1. The substorm onset occurs at Δt = 0 min. (from Wing et al. [2013])

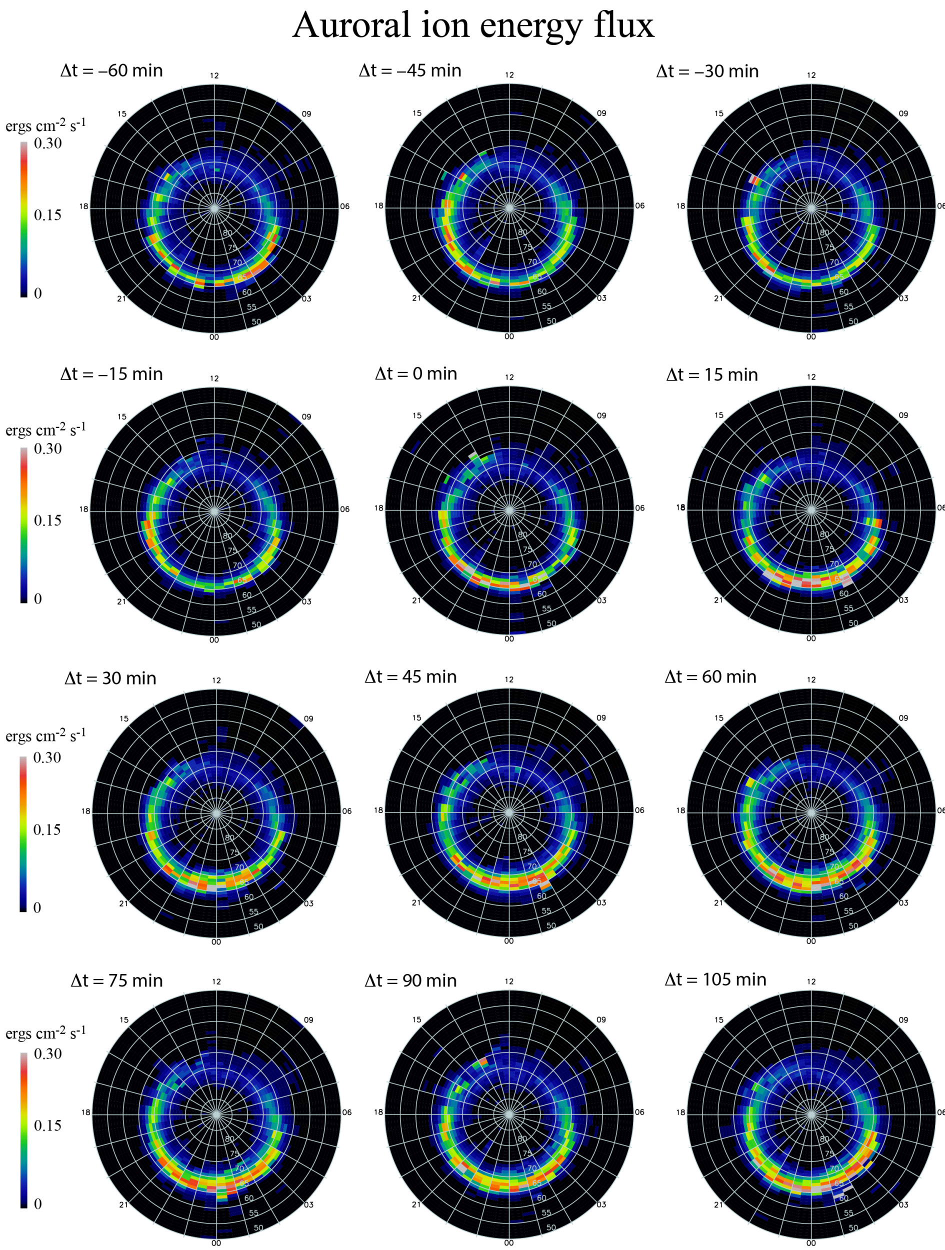

Figure 6. Auroral ion energy flux from 1 hr before to 1 hr and 45 min after the substorm onset in the same format as in Figure 1. The substorm onset occurs at Δt = 0 min. (from Wing et al. [2013])

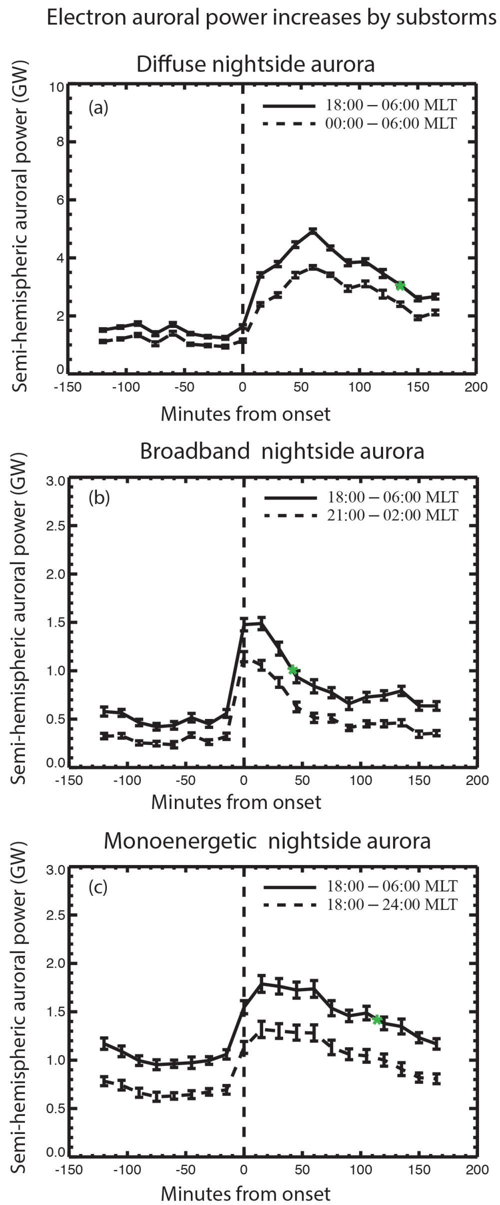

Figure 7. The nightside semihemispheric auroral electron power spanning the interval 2 hr before to 3 hr after substorm onset for (a) diffuse, (b) broadband, and (c) monoenergetic electrons. The solid line shows the entire nightside power obtained from integrating the electron powers in all bins in 18:00–06:00 MLT and 50º–90º MLat. The electron power in each bin is computed by multiplying the physical surface area of each grid by the median energy flux in each bin in Figures 1, 3, and 5. For example, each image in Figure 1 contributes one point on the solid line in (a). The error bars are the standard deviations of the median [e.g., Kenney and Keeping, 1951; Hodges and Lehmann, 1967]. (a) The dashed line shows the midnight–dawn powers obtained from integrating the electron power in all bins in 00:00–06:00 MLT and 50º–90º MLat. (b) The dashed line shows the power obtained by integrating all powers in all bins in 21:00–02:00 MLT and 50º–90º MLat. (c) the dashed line shows the dusk-midnight sector power obtained from integrating the powers in all bins 18:00–24:00 MLT and 50º–90º MLat. The time it takes to reach half maximum power (green asterisks) from the end of the expansion phase (maximum power) for the diffuse (a), broadband (b) and monoenergetic (c) electrons are ~1.2, ~0.42, and 1.6 hr, respectively. (adapted from Wing et al. [2013]).

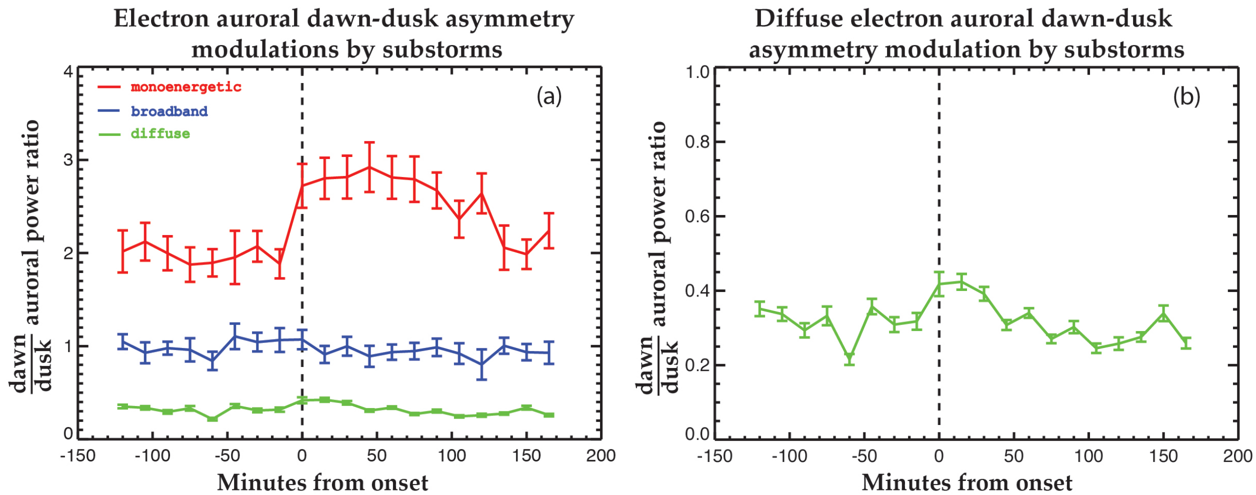

Figure 8. Electron auroral power dawn-dusk asymmetries modulations by substorms. (a) the ratio of dawn (18:00 – 2400 MLT) to dusk (24:00 – 06:00 MLT) auroral power for monoenergetic (red), broadband (blue), and diffuse (green) electrons. The monoenergetic electron auroral power is larger at dawn than at dusk and this asymmetry increases after substorm onset. The asymmetry does not get back to its growth phase value until ~135 min after onset. In contrast, broadband electron auroral power does not show much dawn-dusk asymmetry. The diffuse electron auroral power has the opposite asymmetry from that of monoenergetic electron auroral power (the ratio < 1). At 0 – 30 min after substorm onset, the diffuse electron auroral power dawn-dusk asymmetry decreases a bit. This can be seen more clearly in (b), which plots the same dawn/dusk auroral power ratio as in (a), except that the scale of the Y-axis is smaller.